The influence of channel anion identity on the high-pressure crystal structure, compressibility, and stability of apatite

Richard Skelton[1] , Andrew M. Walker[2]

†   Richard Skelton

richard.skelton@anu.edu.au

[1]   Research School of Earth Sciences, Australian National University, Canberra, ACT, 0200,

Australia

[2]   School of Earth and Environment, University of Leeds, Leeds, LS2 9JT, UK

Abstract The material properties of the common phosphate mineral apatite are influenced by the

identity of the channel anion, which is usually F^-, Cl^-, or $(OH)^-$. Density functional theory

calculations have been used to determine the effect of channel anion identity on the compressibility

and structure of apatite. Hydroxyapatite and fluorapatite are found to have similar zero pressure

bulk moduli, of 79.2 and 82.1 GPa, respectively, while chlorapatite is considerably more

compressible, with K_0 = 55.0 GPa. While the space groups of hydroxyapatite and fluorapatite do not

change between 0 and 25 GPa, symmetrization of the Cl^- site in chlorapatite at ~7.5 GPa causes the

space group to change from $P2_1/b$ to $P6_3/m$. Examination of the valence electron density

distribution in chlorapatite reveals that this symmetry change is associated with a change in the

coordination of the Cl^- anion from 3-fold to 6-fold coordinated by Ca. We also calculate the

pressure at which apatite decomposes to form tuite, a calcium orthophosphate mineral, and find that

the transition pressure is sensitive to the identity of the channel anion, being lowest for fluorapatite

25 (13.8 GPa) and highest for chlorapatite (26.9 GPa). Calculations are also performed within the DFT-

26 D2 framework to investigate the influence of dispersion forces on the compressibility of apatite

27 minerals.

28

35

36

Introduction

38

39 The major host mineral for phosphorus in the Earth's crust and upper mantle is apatite, a calcium

40 phosphate mineral with composition $Ca_{10}(PO_4)_6X_2$, where the channel anion, X, is typically F^-, OH^-,

41 or Cl^- (Pan and Fleet 2002). In addition to being the primary ore for phosphorous, apatite is the most

42 important mineral in the global phosphorous cycle, and can help transport incompatible elements

43 such as the rare earth elements (REEs) and large lithophile elements (LILEs) into the Earth's mantle

44 (Konzett et al. 2012). Apatites are also the major mineral components in animal bones and teeth,

45 and their mechanical and chemical properties play a prominent, if poorly understood role in tooth

46 durability (eg. Menendez-Proupin et al. 2011). Because of this, medical implants are often coated in

47 apatite to improve biocompatibility (Elsinger and Leal 1996; Moore et al. 2001). Natural apatites

48 can contain high concentrations of actinides, and for this reason apatite has been proposed as a

49 potential solid state host for the long-term storage of waste radio-nuclides produced by nuclear

50 reactors (e.g. Arey et al. 1999).

51   The prototypical calcium apatite unit cell, shown in Fig. 1, is hexagonal with space group

52 $P6_3/m$. Each unit cell contains 10 Ca^{2+} ions, which are distributed between two crystallographically

53 distinct cation sites, labeled CaI and CaII. The CaI sites, of which there are four, are 6+3

54 coordinated by O^{2-}, while the six CaII sites, which are arranged in triangles around the channel site,

55 are highly asymmetric, with six Ca-O bonds and one Ca-X bond. To minimize interactions between

56 Ca ions, adjacent CaII triangles (along [0001]) are rotated relative to one another by 60°. The

57 channel sites are typically occupied by either F^- (fluorapatite or FAP), OH^- (hydroxyapatite or

58 HAP), or Cl^-, (chlorapatite or CAP). However, other anions may occupy these sites under certain

59 conditions, most notably oxygen (Trombe and Montel 1978), carbonate (Comodi and Liu 2000) and

60 hydrogen-carbonate (Fleet and Yiu 2007). The identity of the channel anion has a significant

61 influence on the crystal structure of apatite. Changing the channel anion species can even change

62 the crystal symmetry and, while FAP only exists in hexagonal form with space group $P6_3/m$, both

63 HAP (Elliott et al. 1973, Ikoma et al. 1999, Ma and Liu 2009) and CAP (Mackie et al. 1972) have

64 monoclinic variants, although . Due to their large, high-coordination cation sites and isolated PO_4

65 tetrahedra, the apatite crystal can accommodate significant distortion and is thus able to host high

66 concentrations of a wide range of elements, including rare earth elements (REEs) and actinides.

67 This makes apatite important in geochemistry, as its presence can significantly alter REE trends in

68 igneous rocks (eg. Watson and Capabianco 1981).

69   Although the influence of the channel anion identity on the properties apatite is well

70 established at ambient conditions using theoretical calculations (eg Calderin et al. 2003; Rulis et al.

71 2004), the relationship between channel anion identity and the compressibility and high-pressure

72 properties of apatite remains poorly understood. X-ray diffraction studies on HAP, FAP, and CAP

73 indicate that the channel anion affects the compressibility of apatite, with CAP having the lowest

74 bulk modulus, while those of HAP and FAP are similar (Brunet et al. 1999). The measured

75 compressibilities of synthetic lead fluorapatite ($Pb_{10}(PO4)_6F_2$) and lead bromapatite ($Pb_{10}(PO_4)_6F_2$)

76 suggest that the channel anion also influences fine features of the response to pressure, such the

77 ratio of the *a* and *c* cell parameters, *a/c*, a measure of the anisotropy of compression, which is

78 largely pressure independent for lead fluorapatite (Fleet et al. 2010), but decreases moderately with

79 increasing pressure in lead bromapatite (Liu et al. 2011). Intriguingly, both studies found

80 compressibility anomalies at high pressure, suggesting a change in the compression mechanism.

81   In experiments, apatite disproportionates at moderately high pressure to form tuite, γ-

82 $Ca_3(PO_4)_2$, a high density calcium orthophosphate, plus an additional phase which depends on the

83 channel anion identity, typically either CaX_2 (X=F, OH, or Cl), or CaO and a fluid phase (for HAP),

84 and it is thought that this the route by which tuite may form in the mantle (Murayama et al. 1986).

85 Tuite formed by this process could be important for the trace element inventory of the mantle (Zhai

86 et al. 2014; Skelton and Walker 2017). However, the pressure at which apatite reacts to form tuite

87 varies between studies, from as low as 7.5 GPa (Konzett and Frost 2009) to as high as 12 GPa

88 (Murayama et al. 1986).

89   In this study, we use quantum mechanical calculations, with and without dispersion

90 corrections, to determine the effect of pressure on the crystal structures of HAP, FAP, and CAP,

91 obtaining the relaxed atomic structures, cell shapes, and cell volumes of the hexagonal phases of

92 HAP, CAP, and FAP in the range 0-25 GPa. Additionally, we computed enthalpies for the

93 monoclinic variants of CAP and HAP, to determine the pressure dependence of the hexagonal to

94 monoclinic phase transition. Valence electron densities were obtained at a range of pressures,

95 showing the effect of pressure on the bond topology of apatite. Ultimately, it is hoped that these

96 calculations will help shed light on the radically divergent high-pressure behavior of the different

97 apatite minerals.

98

99

Methodology

101

102 We studied the properties of apatite using plane-wave density functional theory (DFT, Hohenberg

103 and Kohn, 1964; Kohn and Sham, 1965), which is a mean-field approach to solving the Schrödinger

104 equation, as implemented in version 5.2 of the Quantum Espresso software package (Giannozzi et

105 al. 2009). The exchange-correlation (xc) energy was treated using the PBE generalized gradient

106 approximation (GGA) xc-functional (Perdew et al. 1996).

107   All calculations were performed using a kinetic energy cutoff of 60 Ry (~816 eV), with

108 reciprocal space sums carried out using Monkhorst-Pack scheme (Monkhorst and Pack 1976), with

109 grid sizes of 2x2x2 and 2x1x2 for the hexagonal and monoclinic apatites, respectively. These values

110 were found to be sufficient to converge the total energy of the simulation cell to <5 meV/atom.

111 Ionic cores were treated using Vanderbilt ultrasoft pseudopotentials (Vanderbilt 1990), which are

112 smoother than regular norm-conserving pseudopotentials and hence require fewer plane waves for

113 accurate calculations. Valence configurations were $3s^2 3p^6 4s^2$, $3s^2 3p^3$, $3s^2 3p^5$, $2s^2 2p^4$, $2s^2 2p^5$, and $1s^1$

114 for Ca, P, Cl, O, F, and H, respectively. At each pressure, the crystal structure was determined by

115 simultaneously relaxing the cell parameters and atomic positions using the BFGS quasi-Newton

116 scheme (Pfrommer et al. 1997). In order to accommodate possible transitions between high- and

117 low-symmetry apatite structures, no symmetry was imposed on the calculations.

118   To determine the effect of channel anion identity on the pressure at which apatite

119 decomposes to form tuite, the enthalpy of the following decomposition reaction is computed:

120 $$Ca_{10}(PO_4)_6 X_2 \rightleftharpoons CaX_2 + 3 Ca_3(PO_4)_2 \tag{1}$$

121 where X=F, Cl, or OH. Murayama et al. (1986), in synthesizing tuite at high pressure and

122 temperature, found that the CaF_2 produced by decomposition of FAP was a solid phase, and that

123 crystalline $Ca(OH)_2$ was produced during decomposition of HAP, at least below 1273 K, above

124 which the decomposition products should be CaO and H_2O. As the calculations here are performed

125 at static conditions (ie. at 0 K), and since the enthalpies of fluid phases cannot be easily computed

126 with DFT, only decomposition reactions which produce tuite and solid CaX_2, (X=F, OH, Cl) are

127 considered here.

128   The enthalpies for the products of reaction (1) were computed with DFT, with the ionic

129 cores treated using the same set of pseudopotentials as were used for apatite. The kinetic energy

130 cutoff used for apatite (60 Ry) was found to be sufficient to ensure convergence of the total energies

131 of tuite and the CaX_2 phases. For tuite, a 4x4x2 k-point grid was sufficient to guarantee

132 convergence of the total energy to <5meV/atom. CaF_2, $Ca(OH)_2$, and $CaCl_2$ all undergo phase

133 transformations in the pressure interval considered here, and enthalpies were computed for the low-

134 pressure and high-pressure phases. For CaF_2, there is a pressure induced phase transition at ~9 GPa

135 (Qi et al. 2013), from the low density fluorite phase (space group *Fm3m*) to a higher density

136 orthorhombic phase with space group *Pnma*. Converged cell energies were obtained by using a

137 4x4x4 k-point grid for the fluorite phase and a 6x4x4 grid for the high-pressure *Pnma* phase. For

138 low pressure $Ca(OH)_2$ (portlandite, space group *P3m*1), a 6x6x6 k-point grid was sufficient to

139 guarantee convergence of the total cell energy. Like CaF_2, $Ca(OH)_2$ undergoes a phase

140 transformation at high pressure, adopting a structure similar to ZrO_2 baddeleyite (space group $P2_1/c$;

141 Kunz et al. 1996), for which a 4x4x4 k-point grid was used. Finally, $CaCl_2$ also undergoes a phase

142 transformation over the pressure range considered in this study (0-30 GPa), from the low pressure

143 rutile-type phase (space group $P4_2/mnm$) to a high-pressure cotunnite-type phase with space group

144 *Pbcn* (Liu et al. 2007). 6x6x8 and 6x4x4 k-point grids were used for the low and high pressure

145 phases, respectively.

146   The GGA xc-functional fails to fully capture the effects of long-ranged dispersive

147 interactions, which contributes to the well-documented tendency of this xc-functional to

148 overestimate cell volumes (see eg. Otero-de-la-Roza and Luana 2011; Luo et al. 2013). Inclusion of

149   dispersion interactions has been found to be important for layer silicates (Ulian et al. 2013a; Ulian

150   et al. 2014). Their correct treatment is also of more general importance when calculating the

151   properties of ionic materials with DFT, and their inclusion is essential for calculating the correct

152   stable phase of cesium chloride (Zhang et al. 2013). Consequently, we recalculate the atomic

153   positions, cell parameters, and reaction enthalpies for FAP, HAP, and CAP using the DFT-D2

154   approach (Grimme 2006). In this formulation, the energy of a DFT calculation is modified by

155   adding an additional term, representing energy of the long-ranged dispersion interactions, which has

156   the form

157    $$E_{\text{dispersion}} = -s_6 \sum_{i=1}^{N} \sum_{j=1}^{N} f(r_{ij}) \frac{C_6^{ij}}{r^{6_{ij}}}$$ (2)

158   where s_6 is a xc-functional dependent scaling factor, taken to be 0.75 for the PBE xc-functional

159   (Grimme 2006), r_{ij} is the interatomic distance, and C_6^{ij} is a numerical coefficient giving the

160   strength of the dispersion interaction between atoms i and j. In the DFT-D2 scheme, this is given by

161   the expression $C_6^{ij} = \sqrt{C_6^i C_6^j}$, where C_6^i is the dispersion coefficient for atom i. The taper

162   function f is used to prevent double counting of short-ranged dispersive interactions, and is given

163   by

164    $$f(r_{ij}) = \frac{1}{1 + e^{-d(r_{ij}/R_{ij}^{\text{vdw}} - 1)}}$$ (3)

165   where d is a steepness parameters and R_{ij}^{vdw} is the sum of the van der Waals radii of atoms i and j.

166   Since dispersion forces may affect apatite minerals and their high-pressure decomposition products

167   differently, enthalpies for the tuite and CaX_2 phases in reaction (1) are also calculated using DFT-

168   D2.

169

170

171   **Results and Discussion**

172

Influence of channel anion identity on crystal structure

174

175 We begin by examining the relationship between channel anion identity and compressibility of the

176 apatite unit cell (Table 1). Calculated cell volumes, a and c parameters, and a/c ratios are plotted in

177 Fig. 2, where it can be seen that CAP has the largest cell volume and highest compressibility, while

178 HAP and FAP have similar cell volumes and compressibilities at all pressures. To quantify this, the

179 calculated cell volumes are fit to a 3rd order Birch-Murnaghan (BM3) equation of state (EOS)

$$180 \quad P(V) = \frac{3K_0}{2}\left[\left(\frac{V_0}{V}\right)^{7/3} - \left(\frac{V_0}{V}\right)^{5/3}\right] \times \left[1 + \frac{3}{4}\left(K_0' - 4\right)\left(\left(\frac{V_0}{V}\right)^{2/3} - 1\right)\right] \qquad (4)$$

181 where V_0 is the zero pressure volume, K_0 the zero pressure isothermal bulk modulus, and K_0' is

182 the pressure derivative of the bulk modulus at 0 GPa. K_0 and K_0' are covariant, and so we also fit

183 the cell volumes to a second order Birch-Murnaghan EOS, in which K_0' is fixed to 4.0. However,

184 this results in a significant reduction of the goodness of fit for all three apatites. Moreover, whether

185 or not K_0' is allowed to vary, the BM3 EOS gives a poor fit to the cell volume data of CAP. The

186 fitted BM3 EOS parameters are given in Table 2. CAP is the softest of the three apatite minerals,

187 with a K_0 of just 55.0 GPa, while FAP is the stiffest, with $K_0 = 90.7$ GPa. The values for the bulk

188 moduli obtained here are significantly lower than those determined by Brunet et al. (1999), by up to

189 11% in the case of HAP, and the fitted values of V_0 for FAP and HAP are larger than the

190 experimental values, by 3.5 and 3.7 %, respectively. This is a consequence of the underbinding of

191 the GGA exchange correlation functional. The calculated zero-pressure cell volume of HAP (549.5

192 Å^3) is larger than the 532 Å^3 found by Ulian et al. (2013b) using all-electron density functional

193 theory with the B3LYP hybrid functional.

194   The order of the a cell parameter lengths at ambient pressure is a(CAP) > a(HAP) > a(FAP),

195 while the order of the c cell parameters is c(FAP) > c(HAP) > c(CAP). At high pressure, the order

196   of the magnitudes of the *a* cell parameters does not change, while the ordering of *c*(HAP) and

197   *c*(FAP) reverses at ~7.5 GPa. As can be seen from the *a/c* ratios of the three apatites (Fig. 2d), the *a*

198   cell axis is more compressible than the *c* axis, as the *a/c* ratio is strictly decreasing with pressure.

199   The magnitude of this decrease is greatest in the case of CAP. This is consistent with the finding of

200   He et al (2012), that the incorporation of large radius ions into the apatite structure dilates the *a* axis

201   more than the *c* axis, increasingly the relative compressibility of the *a* axis. To give a quantitative

202   indication of the relative stiffness of the crystal axes of the different apatite minerals, we fit the

203   BM3 EOS (equation 4) to the cubes of each cell parameter. For the *a* cell parameters, this give

204   effective bulk moduli K_0 of 68.0(16), 60.3(20), and 37.1(21) GPa and $K_0^{'}$ of 4.7(2), 4.9(2), and

205   5.6(3) for FAP, HAP, and CAP, consistent with the ordering found for the total cell volumes. Fitting

206   the cubes of the *c* cell parameters of FAP and HAP (excluding HAP at 0 GPa, where the curvature is

207   apparently negative) gives bulk moduli of 135.6(42) and 158.9(45) GPa and $K_0^{'}$ of 4.5(4) and

208   3.4(3) for FAP and HAP, respectively. For CAP, no meaningful fit parameters can be obtained, due

209   to the anomalous stiffening of the *c*-axis at ~7.5 GPa, a result which explains the poor fit obtained

210   for the cell volumes.

211   This anomaly manifests in the increase of the *z*-coordinate of the Cl^- ion with pressure, from

212   0.398 at 0 GPa to effectively 0.5 at 7.5 GPa, as can be seen in Fig. 3. This corresponds to the Cl^- ion

213   being situated exactly halfway between adjacent CaII triangles. This change in compression

214   mechanism is also associated with a change of space group, which is determined using the program

215   FINDSYM (Stokes and Hatch, 2005), from *P6₃* at low pressure to *P6₃/m* at high pressure. This

216   transition is associated with a change in the Wyckoff site occupied by the Cl^- anion, from *2a* to *2b*.

217   Since the z-coordinate approaches 0.5 continuously, but its pressure derivative is discontinuous

218   where the Wyckoff site changes from *2a* to *2b*, the transition from the *P6₃* to *P6₃/m* space group is

219   of second order.

220   Among the apatites considered in this study, this high-pressure transition appears to be

221   unique to CAP, as no similar compressibility anomalies can be seen for either FAP or HAP. In the

222   former case, the F⁻ ion remains at z = 0.25 (ie. in the center of a CaII triangle) to 25 GPa. Similarly,

223   in HAP, although the hydroxyl group is displaced along the channel with increasing pressure (Fig.

224   3), the pressure derivatives of the O^{2-} or H^+ coordinates do not vary between 0 and 25 GPa. In

225   principle, this could change at pressures substantially above 25 GPa but, as will be shown below,

226   HAP decomposes at high pressure, which means that any such change in the compression

227   mechanism does not fall within its pressure-stability range.

228   Unsurprisingly, given the wildly divergent pressure response of the cell parameters for the

229   three apatites, we find that the influence of pressure on the channel is depends strongly on the

230   identity of the channel anion. To illustrate this, we use the trigonally distorted whose six corners are

231   the Ca^{2+} atoms from two adjacent CaII triangles and which is centered on a hypothetical ion at z =

232   0.5 (Fig. 4a), commonly called the "channel polyhedron" (Fleet et al. 2010). By taking this point to

233   be the center of the polyhedron, we separate the displacement of the channel anion from the

234   distortion of the shape of the channel. At high pressure the channel polyhedron corresponds to the

235   coordination polyhedron of the Cl⁻ anion in CAP. As can be seen from Fig. 4b, the pressure

236   dependence of the channel polyhedron's volume varies greatly between FAP, HAP, and CAP.

237   Furthermore, the channel anion identity also affects the shape of the channel polyhedron, as can be

238   seen from the bond angle variance (BAV; Robinson et al. 1971), which is a measure of the angular

239   distortion of the coordination polyhedron, defined as

240    $$\sigma^2 = \frac{1}{m-1} \sum_{i=1}^{m} (\theta_i - \theta_0)^2 \qquad (5)$$

241   where m is equal to 3/2 times the number of faces in the polyhedron. The θ_i are the bond angles

242   made by two Ca atoms at the vertices of the coordination polyhedron with the site at its center, and

243   θ_0 is the ideal bond angle for a regular polyhedron with $2m/3$ faces. BAV values for the channel

244   polyhedra in FAP, CAP, and HAP are plotted in Fig. 4c. For both FAP and HAP, the BAV of the

10

245 channel polyhedron increases steadily with pressure, although the BAV is somewhat greater for

246 FAP, which may be because the channel anions in FAP (ie. F⁻) remain in the faces of the channel

247 polyhedra at all pressures.

248   The pressure dependence of the shape and compressibility of the CAP channel polyhedron is

249 markedly different from the other apatites. In particular, whereas BAV values for HAP and FAP are

250 monotonic increasing, the BAV of the channel polyhedron in CAP decreases rapidly at low

251 pressure, from 9.47 (°)^2 at 0 GPa to <0.1 (°)^2 at 7.5 GPa. Thereafter, it increases steadily with P, at a

252 rate similar to that of the BAV for the FAP channel polyhedron. At 0 GPa, the channel polyhedron

253 in CAP is substantially larger than those of HAP or FAP. However, its compressibility is also much

254 greater and, above 15 GPa, the channel polyhedra of CAP and HAP have similar volumes and

255 compressibilities. These differences can be quantified by fitting a BM3 EOS to the calculated

256 polyhedral volumes. From this, we find that V_0 = 38.6(2), 34.44(3), and 32.58(1) Å^3 for CAP, HAP,

257 and FAP, respectively, consistent with Cl⁻ being the largest of the channel anions and F⁻ the smallest.

258 Looking now at the bulk modulus and its derivative, we find that, for CAP, K_0 = 28.1(21) GPa and

259    $K_0^{'}$ = 5.5(3). For HAP and FAP, the corresponding values are K_0 = 71.8(11) and 72.4(3) GPa and

260    $K_0^{'}$ = 3.3(1) and 4.53(3), respectively.

261   The contrasting response to pressure can also be seen by examining the internal parameters

262 of the apatite cell. One quantity of particular interest is the metaprism twist ϕ, which is the angle

263 between the projections of the CaI-O1 and CaI-O2 bonds onto (0001) (illustrated in Fig. 5a). This

264 quantity is known to be sensitive to apatite composition, and is consequently used as a probe for

265 chemical composition and order (Lim et al. 2011). For FAP, the metaprism twist increases from

266 22.67° at 0 GPa, compared with the value of 24.3° found by Lim et al. (2011). The metaprism twist

267 angle increases with pressure, reaching a maximum of 23.38° at 7.5 GPa, before declining steadily

268 to 22.80° at 25 GPa. Similarly, for HAP, the value of ϕ increases from 21.57° at 0 GPa, rather less

269 than the value of 23.2° found by Sudarsanan and Young (1972), reaching a maximum value of

270 23.05° at 10.0 GPa, and decreasing to 22.63° by 25 GPa. While the range of angular values is

271 somewhat greater in HAP than in FAP, in both cases the metaprism twist is only weakly dependent

272 on pressure. However, as can be seen in Fig. 5a, the effect of pressure on the metaprism twist angle

273 in CAP is radically different, with ϕ increasing rapidly from a value of just 14.37° at 0 GPa, to

274 20.21° at 22.5 GPa, declining slowly thereafter. Note that, as for the other two apatites, ϕ is rather

275 less than the experimentally determined value of 17.8° (Sudarsanan and Young 1980). However, the

276 relative magnitudes of the metaprism twist angles is reproduced successfully, with ϕ(CAP) <

277 ϕ(HAP) < ϕ(FAP).

278   Another measure of the response of the apatite crystal structure to pressure is the X-X-CaII

279 angle (illustrated in Fig. 5*b* for FAP). This quantity, referred to hereafter as the "skew" angle ψ,

280 measures the rotation of the channels relative to one another. If the channels are lined up perfectly

281 should be exactly 120°. Indeed, from Fig. 5*b* it can seen that, at 0 GPa, this is very nearly the case

282 for FAP and HAP, for which the values of are 120.02° and 119.51°, respectively. However, the

283 effect of increasing pressure is to rotate the channels relative to one another such that, at 25 GPa,

284 the calculated values of *y* are 123.35° for FAP and 123.46° for HAP. As was the case for the

285 metaprism twist, the effect of pressure on the skew angle is rather more pronounced for CAP, for

286 which ψ increases from 115.82° at 0 GPa to 122.32° at 25 GPa.

287   The differences in the high-pressure responses of the different apatites is apparent not only

288 in the crystal structure but also in the bond topology in the vicinity of the channel. This can be seen

289 in the differences between the low- and high-pressure valence electron density distributions of HAP

290 with those of CAP, shown in Fig. 6. In the former, although the channel site shrinks and the

291 hydroxyl group is progressively displaced along the *c*-axis, the bond topology remains unchanged,

292 with the hydroxyl oxygen three-fold coordinated to Ca^{2+} at all pressures between 0 and 25 GPa. At 0

293 GPa, the electron density distribution of CAP looks very similar to that of HAP, with each Cl^{-} anion

294 in CAP sharing substantial electron density with Ca^{2+} ions in a only single layer, for a total effective

295 coordination number of three. However, at high pressure the Cl^- anion has clearly defined bonds

296 with all Ca^{2+} ions in the CaII triangles both above and below it, raising the effective coordination

297 number to six. Simultaneously, the channel site symmetrizes, and a mirror planes develop at z =0.25

298 and z =0.75, halfway between adjacent Cl^- anions. This symmetrization coincides with (indeed,

299 causes) the substantial stiffening of the CAP *c*-axis seen at ~7.5 GPa in Fig. 2*c*, and the associated

300 anomaly in the *a*/*c* compression ratio (Fig. 2d).

301 A similar anomaly in the *a*/*c* compression ratio has also been observed in synthetic lead

302 fluorapatite (PbFAP; Fleet et al. 2010). Diffraction data shows that, at ambient pressure, the channel

303 ion in PbFAP, much like the channel anions in HAP and CAP, is displaced along [0001] to z =

304 0.461. While Fleet et al. (2010) were unable to refine the location of the F^- ion at high pressure, as

305 F^- is much lighter than Pb^{2+} and hence difficult to locate in x-ray diffraction, the observed changes

306 in the *a*/*c* compressibility ratio and the substantially greater compressibility of the channel

307 polyhedron are consistent with progressive displacement of the channel anion along [0001] that

308 stalls as the anion approaches z = 0.5, as was found to be the case here for Ca-CAP. This may also

309 explain similar compressibility anomalies in lead bromapatite (PbBrAp; Liu et al. 2011).

310

311 **The effect of dispersion forces on the high-pressure structure of apatite**

312

313 The larger cell volumes and lower zero-pressure bulk modulus of apatite, relative to experiments,

314 reported in the previous section can be attributed to the use of the PBE-GGA xc-functional, which is

315 known to significantly underbind. While several factors contribute to this underbinding, one

316 potentially important source is the failure of the PBE-GGA xc-functional to adequately model long-

317 ranged dispersive interactions. To determine the significance of this for apatite compressibility, cell

318 volumes and cell parameters were calculated using the DFT-D2 approach, as described above.

319   Calculated a and c cell parameters and cell volumes for FAP, HAP, and CAP are reported in Table 3

320   and plotted in Fig. 7, the inclusion of dispersion forces via the DFT-D2 scheme reduces the cell

321   volumes of all apatites considered here, as well as both the a and c cell parameters.

322   The significance of this reduction can be quantified by fitting the BM2 and BM3 equations

323   of state to the cell volumes calculated with DFT-D2. The fitted parameters are reported in Table 4.

324   The inclusion of dispersion forces does not affect the ordering of the compressibilities of the three

325   minerals, with CAP and FAP remaining the most and least compressible minerals, respectively.

326   However, the DFT-D2 BM2 fit parameters are substantially closer to those obtained by Brunet et al.

327   (1999) for natural apatites, particularly for FAP, whose fitted BM2 K_0 is within error of the value

328   reported by Brunet et al. (1999). The zero-pressure cell volume V_0 is also substantially better

329   reproduced by the DFT-D2 calculations, with the calculated values for FAP and HAP just 1.3% and

330   1.4% greater than those obtained by Brunet et al. (1999) by fitting to experimental data.

331   The inclusion of dispersion forces through the DFT-D2 also influences the response of the a

332   and c cell parameters to pressure. As was done in the previous section for the PBE-GGA

333   calculations, the relative stiffness of the crystal axes can be quantified by fitting the cubes of their

334   values to a BM3 EOS (equation 4). For the a cell parameters, the zero-pressure bulk moduli K_0 are

335   79.4(3), 73.4(4), and 63.4(11) GPa for FAP, HAP, and CAP, respectively, while the corresponding

336   derivatives $K_0^{'}$ are 4.1(1), 4.2(1), and 4.2(1). For the cubes of the c cell parameters, the BM3

337   EOS fit parameters are K_0 = 132.3(4) and 147.4(17) GPa and $K_0^{'}$ = 5.7(1) and 4.5(1) for FAP and

338   HAP, respectively.

339   As was found in preceding section using DFT without a dispersion correction, the c cell

340   parameter cannot be meaningfully fitted to a BM3 EOS, as the c axis compressibility changes at

341   ~7.5 GPa. From Fig. 7c, it can be seen that the DFT-D2 calculations predict that, in contrast to the

342   DFT calculations, the c axis actually softens as it approaches this pressure, and then stiffens

343   considerably above it. This anomaly in the c axis compressibility can, as in the DFT results, be

344 attributed to the progressive increase of the z-coordinate of the Cl$^-$ ion with pressure. At 0 GPa, the

345 z-coordinate is 0.449, greater than the value obtained using DFT with no dispersion correction.

346 However, the DFT-D2 calculations predict a lower pressure sensitivity of the z-coordinate of the Cl$^-$

347 anion, so that the Cl- anion reaches the site halfway between adjacent CaII triangles at

348 approximately the same pressure as was predicted from DFT calculations without a dispersion

349 correction (ie. ~7.5 GPa). It is likely that this accounts for the qualitatively different response of the

350 c axis to increasing pressure below the P6$_3$ → P6$_3$/m transition predicted by the DFT and DFT-D2

351 calculations, with the anomaly in the a/c ratios being more pronounced in the latter case, as can be

352 seen by comparing Fig. 2c and Fig. 7c). We use FINDSYM (Stokes and Hatch 2005), we determine

353 the space group of CAP, which is determined to change from $P6_3$ to $P6_3/m$ at ~7.5 GPa, similar to

354 the value determined from the dispersion-uncorrected simulations.

355

356 **The monoclinic-hexagonal phase transitions**

357

358 Although only hexagonal apatite structures have so far considered here, both HAP (Elliot et al.

359 1973; Ma and Liu 2009) and CAP (Mackie et al. 1972) are known to have monoclinic symmetry at

360 room pressure. Given the different behavior found for the hexagonal phases of these two apatites, it

361 is likely that the pressure dependence of the boundary between their hexagonal and monoclinic

362 phases will also differ. To test this, we compute enthalpies of the monoclinic phases to 25 GPa and

363 compare the enthalpy changes of the monoclinic to hexagonal phase transitions. In addition, to

364 account for the possibility of a monoclinic FAP phase, the cell has been relaxed with F$^-$ anion

365 initially displaced along the [0001] axis (with opposite sense in adjacent channels) from its position

366 at (0.0, 0.0, 0.25). However, at all pressures, it was found that FAP relaxes to the hexagonal crystal

367 structure with space group $P6_3/m$.

368   As can be seen from Fig. 9, the stability of the monoclinic phase of HAP increases with

369   pressure. This can be attributed to the fact that increasing pressure decreases the distance between

370   adjacent channels, thereby strengthening the coupling between channel sites. In contrast,

371   monoclinic CAP has the same enthalpy as hexagonal CAP above 7.5 GPa. Indeed, analysis of the

372   monoclinic and hexagonal crystal phases using the program FINDSYM (Stokes and Hatch, 2005)

373   shows that they are structurally identical above this pressure (ie. hexagonal with space group $P6_3/m$

374   and the Cl^- ion in the $2b$ Wyckoff site). It is well-established that the underbinding of GGA-type xc-

375   functionals leads to overestimation of transition pressures. Consequently, the stability of monoclinic

376   HAP relative to the hexagonal phase should be somewhat greater at constant pressure predicted

377   using just the PBE-GGA xc-functional. The inclusion of dispersion forces using the DFT-D2

378   scheme has no substantial effect on the relative stabilities of the monoclinic and hexagonal phases,

379   although the enthalpy difference between the hexagonal and monoclinic variants of HAP increases,

380   from 0.02 eV/ hexagonal cell to 0.06 eV/hexagonal cell at 0 GPa and 0.11 eV/hexagonal cell to 0.19

381   eV/hexagonal cell at 25 GPa. The energy difference between the monoclinic and $P6_3$ hexagonal

382   forms of CAP at 0 GPa calculated with DFT-D2 (0.06 eV/hexagonal cell) is also slightly higher

383   than the ΔH of 0.02 eV/hexagonal cell calculated without a dispersion correction. While the energy

384   difference between monoclinic and hexagonal cells is calculable, we note that the values are not

385   large, which means that the orientations of adjacent channels are not tightly coupled.

386   Previous studies have suggested that hydroxyapatites may have ordered channels.

387   Disordering of the orientations of the $(OH)^-$ groups in the channels has been proposed to be

388   responsible for the high-T transition from $P2_1/b$ to $P6_3/m$ (Hochrein et al. 2005). However, de

389   Leeuw (2010) noted that the coupling energy between adjacent columns is relatively small.

390   Consequently, increasing the temperature should mean that, while the hydroxyl groups within a

391   channel should remain ordered, the orientations of the hydroxyl groups in adjacent channels are no

392   longer correlated. This increases the symmetry of the crystal from $P2_1/b$ to $P6_3/m$. In this model, the

16

393 disordering temperature depends (to first order) on the coupling between channels, which is roughly

394 proportional to the relative stability of the monoclinic and (ordered, ie. $P6_3$) hexagonal phases.

395 Consequently, from the relative stabilities of the hexagonal and monoclinic phases calculated in this

396 study, it is expected that the temperature at which the transition from monoclinic to hexagonal HAP

397 occurs should increase with pressure.

398   By the same reasoning, CAP should form the disordered (ie. $P6_3/m$) hexagonal phase at

399 progressively lower temperatures as the pressure increases. The symmetrization of the channel site

400 at high pressure means that the monoclinic phase can no longer exist, and above the transition

401 pressure CAP will have the ordered hexagonal structure (with Cl at z=0.5) at all temperatures where

402 apatite is stable. More detailed analysis on the effect of pressure on the temperature of the

403 monoclinic to hexagonal phase transition would require a study of the free energy change across the

404 phase boundary informed by molecular dynamics or lattice dynamics calculations. However, this is

405 beyond the scope of the present work.

406

407 **The apatite-tuite phase boundary**

408

409 Enthalpies for the reaction whereby apatite decomposes to produce tuite and CaX_2 are calculated

410 from using the enthalpies calculated with PBE-GGA without the DFT-D2 dispersion correction. As

411 discussed in the Methodology section, CaF_2, $Ca(OH)_2$, and $CaCl_2$ all undergo phase transitions in

412 the pressure range considered in study. Consequently, for each pressure, we use the enthalpy of the

413 stable CaX_2 phase at that pressure. Calculated enthalpies for reaction (1) are plotted in Fig. 8, where

414 it can be seen that the formation of tuite is quite sensitive to the identity of the channel anion in

415 apatite, with CAP remaining stable to far higher pressures than either HAP or FAP. The transition

416 pressure is lowest when the channel anion is F and highest when it is Cl, with transition pressures of

417 13.8, 15.5, and 26.9 GPa for FAP, HAP, and CAP, respectively. The ordering of the phase transition

418   pressures is unchanged by the inclusion of a dispersion correction using the DFT-D2 scheme,

419   although their values are reduced modestly to 8.0, 9.6, and 19.3 GPa for FAP, HAP, and CAP. These

420   results suggests that, while HAP and FAP will disproportionate to form tuite + CaX_2 somewhere

421   between the deep upper mantle and the upper transition zone, CAP may potentially remain stable

422   into the lower mantle. In natural apatites, the occupancy of the channel depends on the origin of the

423   apatite, with those in metasomatized mantle peridotites being more Cl^- rich and F^- poor, while those

424   crystallized from magma at high-pressure are relatively F^- rich (O'Reilly and Griffin 2000; O'Reilly

425   and Griffin 2013). Thus, the origin of an apatite crystal may influence the pressure at which it

426   potentially decomposes to form tuite in the mantle.

427   HAP and CAP both have monoclinic polymorphs, which may influence the pressure of the

428   apatite → tuite transition. Given that the monoclinic variant of CAP disappears at pressures well

429   below the calculated apatite → tuite phase boundary, this will not affect the result when X=Cl^-.

430   However, as shown above, in the case of HAP, pressure increases the stability of the monoclinic

431   structure over the hexagonal structure, which will shift the apatite → tuite phase boundary to

432   higher pressures. Nevertheless, as can be seen in Fig. 8, this is a minor effect, and not enough to

433   influence the relative ordering of the high-pressure stabilities for the three apatite compositions. The

434   pressure derivatives of the enthalpies for each of the three apatites are nearly identical. In contrast,

435   the enthalpy per atom of $CaCl_2$ increases much more rapidly with pressure than either $Ca(OH)_2$ or

436   CaF_2. Consequently, the strong dependence of the decomposition pressure on the channel anion is

437   driven by the enthalpy of the CaX_2 phase, rather than that of apatite.

438   Clearly, the identity of the channel anion has a significant influence on the relative stability

439   of the apatite and tuite assemblages. Indeed, our calculations predict that, while HAP and FAP

440   decompose to form tuite + CaX_2 at pressures comparable to those in the upper transition zone, CAP

441   can remain stable to considerably greater depths. Konzett and Frost (2009) reported the

442   decomposition pressure of hydroxyapatite in a system with a mid-ocean ridge basalt (MORB)

443   composition, finding that tuite was produced at 7.5 GPa, lower than the value reported by

444   Murayama et al. (1986), which is halfway between the values calculated here with DFT and DFT-

445   D2. Similarly, Konzett et al. (2012) reported, in an assemblage containing chlorapatite and

446   phlogopite, tuite formed was present at below 9 GPa, significantly lower than the value reported in

447   this study. In this case, the decomposition products included a Cl-rich fluid, which may be

448   responsible for destabilizing CAP. This suggests that the presence of coexisting phases, whether

449   minerals (Konzett and Frost 2009) or fluids (Konzett et al. 2012), can affect the pressure at which

450   tuite forms from apatite, particularly in the case of CAP. Temperature will also reduce the pressure

451   at which these decomposition reactions occur, but is unlikely to alter their relative order, with FAP

452   decomposing at the lowest pressure and CAP persisting to greater depths.

453

454

455   **Conclusions**

456

457   In this study, *ab initio* calculations were used to examine the effect of different common channel

458   anion species on the compressibility of apatite. It was found that channel anion identity has a

459   substantial influence on the compressibility of apatite, as all three apatites displayed different

460   pressure dependences of the cell parameters, bond lengths, and polyhedral volumes, as well as

461   subtle structural features such as the metaprism twist and channel skew angles. However, the

462   differences between CAP and the other apatites were far more significant those between FAP and

463   HAP. Moreover, the qualitative nature of the compression mechanism varied between the three

464   apatites, with FAP compressing uniformly, HAP compressing through progressive displacement of

465   the hydroxyl groups along the channels. In CAP, meanwhile, the Cl^- shifted along the channel at low

466   pressure, but were constrained by symmetry to remain stationary above 7.5 GPa, greatly increasing

467   the stiffness of the *c*-axis. While the inclusion of dispersion forces using the DFT-D2 method was

468 found to decrease the cell volumes of all three apatites and increase their bulk moduli, the ordering

469 of these parameters was not, nor was the pressure at which the Cl$^-$ site in CAP symmetrizes greatly

470 affected, although the evolution of the CAP *c* axis compressibility below 7.5 GPa does appear to be

471 affected by dispersion forces.

472   This meant that, although the space groups of hexagonal FAP and HAP (*P6$_3$/m* and *P6$_3$*,

473 respectively) do not change over the pressure range studied, hexagonal CAP, whose space group is

474 *P6$_3$* at ambient conditions, has space group *P6$_3$/m* above 7.5 GPa, associated with the development

475 of a mirror planes at z = 0.25 and z = 0.75. This is associated with an increase in the coordination of

476 the Cl$^-$ channel anion from three to six-fold coordinated by the CaII sites. By calculating the

477 enthalpies of the monoclinic structures, it was found that the compression anomaly in CAP

478 coincides with a change in symmetry from monoclinic to hexagonal. While monoclinic HAP

479 becomes more stable than hexagonal HAP with increasing pressure, monoclinic CAP ceases to exist

480 above 7.5 GPa.

481

489

490

491 **References**

492

493   Arey JS, Seaman JC, Bertsch PM (1999) Immobilization of uranium in contaminated sediments by

494   hydroxyapatite addition. Environ Sci Technol 33:337–342. doi: 10.1021/es980425+

495   Brunet F, Allan DR, Redfern SAT, et al. (1999) Compressibility and thermal expansivity of

496   synthetic apatites, $Ca_5(PO_4)_3X$ with X = OH, F and Cl. Eur J Mineral 11:1023–1036. doi:

497   10.1127/ejm/11/6/1023

498   Calderín L, Stott MJ, Rubio A (2003) Electronic and crystallographic structure of apatites. Phys Rev

499   B 67:134106 . doi: 10.1103/PhysRevB.67.134106

500   Comodi P, Liu Y (2000) CO_3 substitution in apatite. Eur J Mineral 12:965–974. doi: 10.1127/0935-

501   1221/2000/0012-0965

502   Elliott JC, Mackie PE, Young RA (1973) Monoclinic hydroxyapatite. Science 180:1055–1057. doi:

503   10.1126/science.180.4090.1055

504   Elsinger EC, Leal L (1996) Coralline hydroxyapatite bone graft substitutes. J Foot Ankle Surg

505   35:396–399. doi: 10.1016/S1067-2516(96)80058-5

506   Fleet ME, Liu X (2007) Letter: Hydrogen-carbonate ion in synthetic high-pressure apatite. Am

507   Mineral 92:1764–1767 . doi: 10.2138/am.2007.2716

508   Fleet ME, Liu X, Shieh SR (2010) Structural change in lead fluorapatite at high pressure. Phys

509   Chem Miner 37:1–9. doi: 10.1007/s00269-009-0305-3

510   Giannozzi P, Baroni S, Bonini N, et al. (2009) QUANTUM ESPRESSO: a modular and open-

511   source software project for quantum simulations of materials. J Phys-Condens Mat

512   21:395502. doi: 10.1088/0953-8984/21/39/395502

513   Hohenberg P, Kohn W (1964) Inhomogeneous electron gas. Phys Rev 136:B864–B871. doi:

514   10.1103/PhysRev.136.B864

515   Grimme S (2006) Semiempirical GGA-type density functional constructed with a long-range

516   dispersion correction. J Comput Chem 27:1787–1799 . doi: 10.1002/jcc.20495

517 He Q, Liu X, Hu X, et al (2012) Solid solutions between lead fluorapatite and lead fluorvanadate

518   apatite: compressibility determined by using a diamond-anvil cell coupled with synchrotron

519   X-ray diffraction. Phys Chem Miner 39:219–226 . doi: 10.1007/s00269-011-0477-5

520 Hochrein O, Kniep R, Zahn D (2005) Atomistic simulation study of the order/disorder (monoclinic

521   to hexagonal) phase transition of hydroxyapatite. Chem Mater 17:1978–1981 . doi:

522   10.1021/cm0401903

523 Ikoma T, Yamazaki A, Nakamura S, Akao M (1999) Preparation and structure refinement of

524   monoclinic hydroxyapatite. J Solid State Chem 144:272–276. doi: 10.1006/jssc.1998.8120

525 Kohn W, Sham LJ (1965) Self-consistent equations including exchange and correlation effects.

526   Phys Rev 140:A1133–A1138. doi: 10.1103/PhysRev.140.A1133

527 Konzett J, Frost DJ (2009) The high P–T stability of hydroxyl-apatite in natural and simplified

528   MORB—an experimental study to 15 GPa with implications for transport and storage of

529   phosphorus and halogens in subduction zones. J Petrol 50:2043–2062 . doi:

530   10.1093/petrology/egp068

531 Konzett J, Rhede D, Frost DJ (2012) The high PT stability of apatite and Cl partitioning between

532   apatite and hydrous potassic phases in peridotite: an experimental study to 19 GPa with

533   implications for the transport of P, Cl and K in the upper mantle. Contrib Mineral Petr

534   163:277–296. doi: 10.1007/s00410-011-0672-x

535 Kunz M, Leinenweber K, Parise JB, et al. (1996) The baddeleyite-type high pressure phase of

536   Ca(OH)2. High Pressure Res 14:311–319 . doi: 10.1080/08957959608201416

537 Leeuw NH de (2010) Computer simulations of structures and properties of the biomaterial

538   hydroxyapatite. J Mater Chem 20:5376–5389 . doi: 10.1039/B921400C

539 Lim SC, Baikie T, Pramana SS, et al. (2011) Apatite metaprism twist angle (φ) as a tool for

540   crystallochemical diagnosis. J Solid State Chem 184:2978–2986. doi:

541   10.1016/j.jssc.2011.08.031

542 Liu X, Fleet ME, Shieh SR, He Q (2011) Synthetic lead bromapatite: X-ray structure at ambient

543   pressure and compressibility up to about 20 GPa. Phys Chem Miner 38:397–406. doi:

544   10.1007/s00269-010-0413-0

545 Liu YH, Ma YM, He Z, et al. (2007) Phase transition and optical properties of $CaCl_2$ under high

546   pressure by ab initio pseudopotential plane-wave calculations. J Phys-Condens Mat

547   19:425225 . doi: 10.1088/0953-8984/19/42/425225

548 Luo F, Cheng Y, Cai L-C, Chen X-R (2013) Structure and thermodynamic properties of BeO:

549   Empirical corrections in the quasiharmonic approximation. J Appl Phys 113:033517 . doi:

550   10.1063/1.4776679

551 Ma G, Liu XY (2009) Hydroxyapatite: hexagonal or monoclinic? Cryst Growth Des 9:2991–2994.

552   doi: 10.1021/cg900156w

553 Mackie PE, Elliot JC, Young RA (1972) Monoclinic structure of synthetic $Ca_5(PO_4)_3Cl$,

554   chlorapatite. Acta Crystall B-Stru 28:1840–1848. doi: 10.1107/S0567740872005114

555 Menéndez-Proupin E, Cervantes-Rodríguez S, Osorio-Pulgar R, et al. (2011) Computer simulation

556   of elastic constants of hydroxyapatite and fluorapatite. J Mech Behav Biomed 4:1011–1020.

557   doi: 10.1016/j.jmbbm.2011.03.001

558 Momma K, Izumi F (2011) *VESTA 3* for three-dimensional visualization of crystal, volumetric and

559   morphology data. J Appl Crystallogr 44:1272–1276. doi: 10.1107/S0021889811038970

560 Moore WR, Graves SE, Bain GI (2001) Synthetic bone graft substitutes. ANZ J Surg 71:354–361.

561   doi: 10.1046/j.1440-1622.2001.02128.x

562 Murayama JK, Nakai S, Kato M, Kumazawa M (1986) A dense polymorph of $Ca_3(PO_4)_2$: a high

563   pressure phase of apatite decomposition and its geochemical significance. Phys Earth Planet

564   In 44:293–303. doi: 10.1016/0031-9201(86)90057-9

565   O'Reilly SY, Griffin WL (2000) Apatite in the mantle: implications for metasomatic processes and

566   high heat production in Phanerozoic mantle. Lithos 53:217–232 . doi: 10.1016/S0024-

567   4937(00)00026-8

568   O'Reilly SY, Griffin WL (2013) Mantle metasomatism. In: Harlov DE, Austrheim H (eds)

569   Metasomatism and the chemical transformation of rock: the role of fluids in terrestrial and

570   extraterrestrial processes. Springer, Berlin, pp 471-533

571   Otero-de-la-Roza A, Luaña V (2011) Treatment of first-principles data for predictive quasiharmonic

572   thermodynamics of solids: the case of MgO. Phys Rev B 84:024109 . doi:

573   10.1103/PhysRevB.84.024109

574   Pan Y, Fleet ME (2002) Compositions of the apatite-group minerals: Substitution mechanisms and

575   controlling factors. In: Kohn MJ, Rakovan J, Hughes JM (eds) Phosphates: Geochemical,

576   geobiological and materials importance. Rev Mineral Geochem, vol 48. Mineral Soc Am,

577   Chantilly, pp 13–50

578   Perdew JP, Burke K, Ernzerhof M (1996) Generalized gradient approximation made simple. Phys

579   Rev Lett 77:3865–3868. doi: 10.1103/PhysRevLett.77.3865

580   Pfrommer BG, Côté M, Louie SG, Cohen ML (1997) Relaxation of crystals with the quasi-Newton

581   method. J Comput Phys 131:233–240. doi: 10.1006/jcph.1996.5612

582   Qi Y-Y, Cheng Y, Liu M, et al. (2013) Phase transition and thermodynamic properties of CaF_2 via

583   first principles. Physica B 426:13–19 . doi: 10.1016/j.physb.2013.05.033

584   Robinson K, Gibbs GV, Ribbe PH (1971) Quadratic elongation: a quantitative measure of distortion

585   in coordination polyhedra. Science 172:567–570. doi: 10.1126/science.172.3983.567

586   Rulis P, Ouyang L, Ching WY (2004) Electronic structure and bonding in calcium apatite

587   crystals: hydroxyapatite, fluorapatite, chlorapatite, and bromapatite. Phys Rev B

588   70:155104 . doi: 10.1103/PhysRevB.70.155104

589   Skelton R, Walker AM (2017) Ab initio crystal structure and elasticity of tuite, γ-Ca$_3$(PO$_4$)$_2$, with

590   implications for trace element partitioning in the lower mantle. Contrib Mineral Petr

591   172:87 . doi: 10.1007/s00410-017-1406-5

592   Stokes HT, Hatch DM (2005) FINDSYM: program for identifying the space-group symmetry of a

593   crystal. J Appl Crystallogr 38:237–238. doi: 10.1107/S0021889804031528

594   Sudarsanan K, Young RA (1972) Structure of strontium hydroxide phosphate, Sr$_5$(PO$_4$)$_3$OH. Acta

595   Cryst B-Stru 28:3668–3670. doi: 10.1107/S0567740872008544

596   Sudarsanan K, Young RA (1980) Structure of partially substituted chlorapatite (Ca$_2$Sr)$_5$(PO$_4$)$_3$Cl.

597   Acta Cryst B-Stru 36:1525–1530. doi: 10.1107/S0567740880006516

598   Trombe JC, Montel G (1978) Some features of the incorporation of oxygen in different oxidation

599   states in the apatitic lattice—I On the existence of calcium and strontium oxyapatites. J

600   Inorg Nucl Chem 40:15–21. doi: 10.1016/0022-1902(78)80298-X

601   Ulian G, Tosoni S, Valdrè G (2013a) Comparison between Gaussian-type orbitals and plane wave

602   ab initio density functional theory modeling of layer silicates: Talc [Mg$_3$Si$_4$O$_{10}$(OH)$_2$] as

603   model system. J Chem Phys 139:204101 . doi: 10.1063/1.4830405

604   Ulian G, Valdrè G, Corno M, Ugliengo P (2013b) Periodic ab initio bulk investigation of

605   hydroxylapatite and type A carbonated apatite with both pseudopotential and all-electron

606   basis sets for calcium atoms. Am Mineral 98:410–416. doi: 10.2138/am.2013.4171

607   Ulian G, Tosoni S, Valdrè G (2014) The compressional behaviour and the mechanical properties of

608   talc [Mg$_3$Si4O$_{10}$(OH)$_2$]: a density functional theory investigation. Phys Chem Miner 41:639–

609   650 . doi: 10.1007/s00269-014-0677-x

610   Vanderbilt D (1990) Soft self-consistent pseudopotentials in a generalized eigenvalue formalism.

611   Phys Rev B 41:7892–7895. doi: 10.1103/PhysRevB.41.7892

612   Watson EB, Capobianco CJ (1981) Phosphorus and the rare earth elements in felsic magmas: an

613   assessment of the role of apatite. Geochim Cosmochim Ac 45:2349–2358. doi:

614   10.1016/0016-7037(81)90088-0

615   Zhai S, Xue W, Yamazaki D, Ma F (2014) Trace element composition in tuite decomposed from

616   natural apatite in high-pressure and high-temperature experiments. Sci China Earth Sci

617   57:2922–2927 . doi: 10.1007/s11430-014-4980-7

618   Zhang F, Gale JD, Uberuaga BP, et al. (2013) Importance of dispersion in density functional

619   calculations of cesium chloride and its related halides. Phys Rev B 88:054112 . doi:

620   10.1103/PhysRevB.88.054112

621

622

Figure captions

624
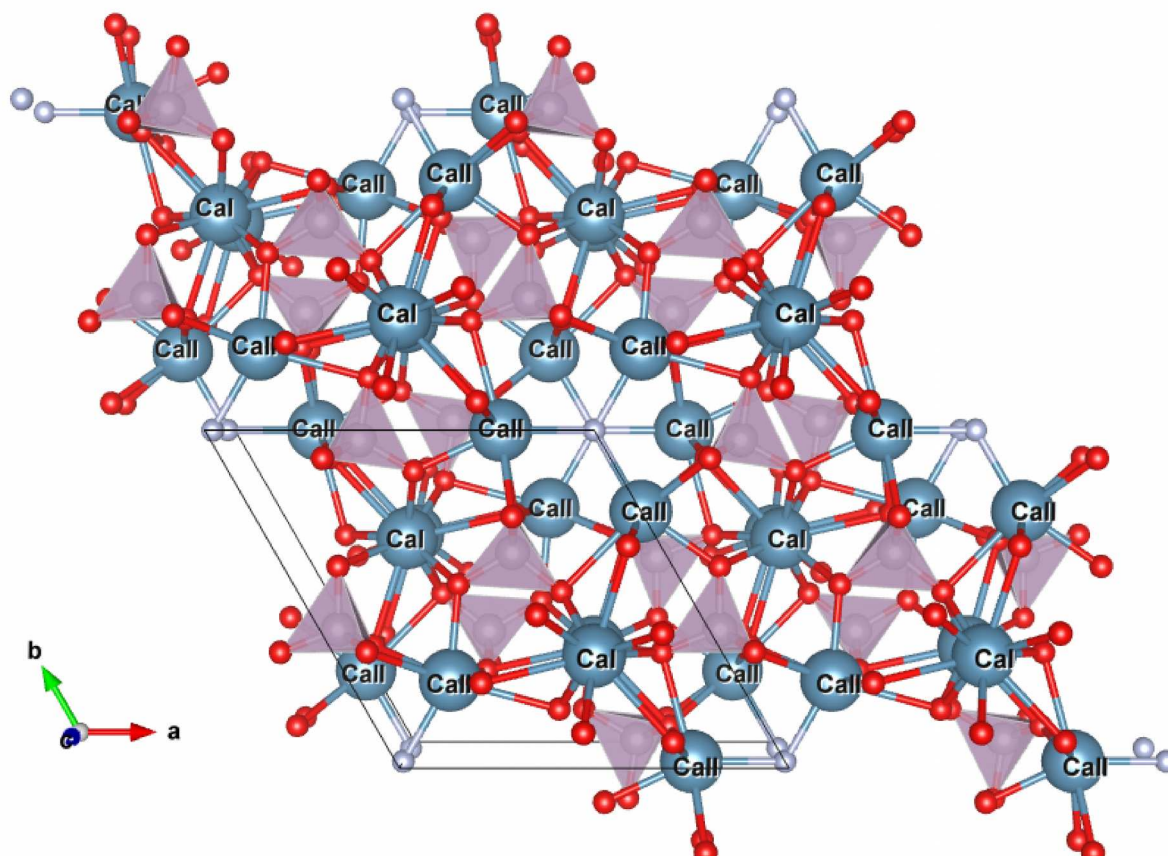
Fig. 1 Crystal structure of apatite, viewed down the [0001] axis. Image produced using the crystal structure visualization software VESTA 3 (Momma and Izumi 2011)
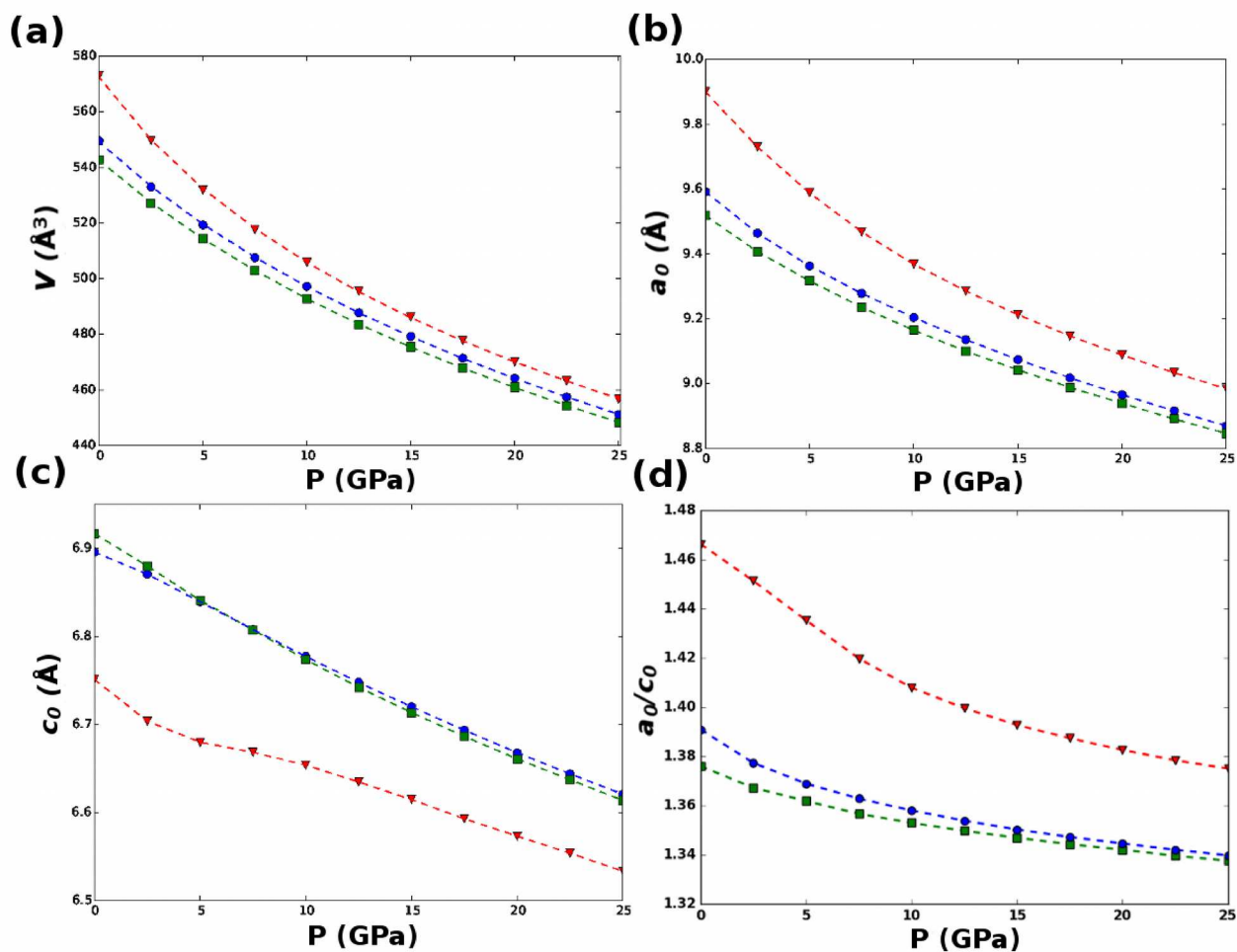
627

628 **Fig. 2** Pressure dependence of the (a) cell volumes, (b) a_0 cell parameters, (c) c_0 cell parameters, and

629 (d) a_0/c_0 ratios of FAP (squares), HAP (circles), and CAP (inverted triangles)

630
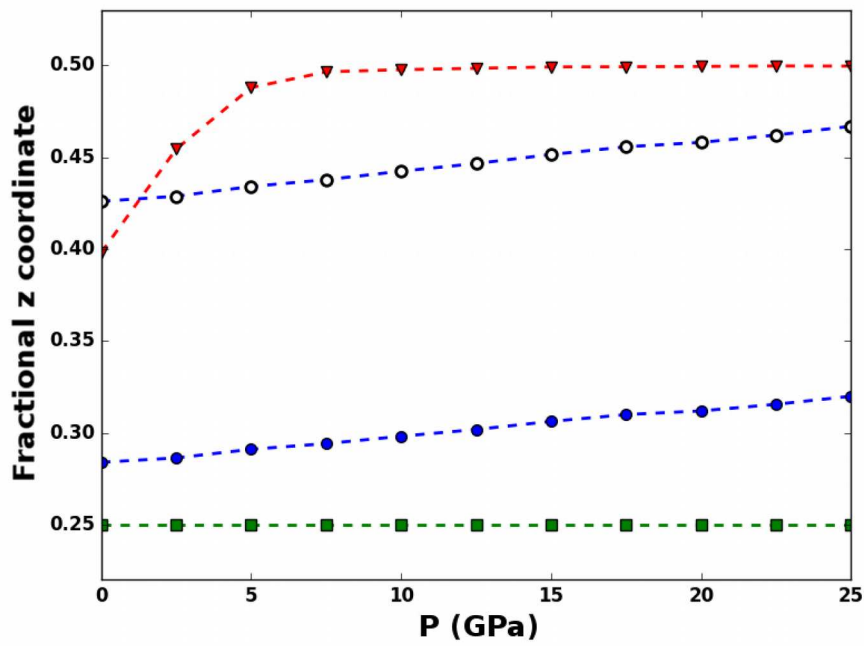
631

632 **Fig. 3** Plot of the pressure dependence of z-coordinates of the F^- anion in FAP (squares), the Cl^-

633 anion in CAP (inverted triangles), and the O^{2-} (filled circles) and H^+ (hollow circles) ions in the

634 $(OH)^-$ group of HAP
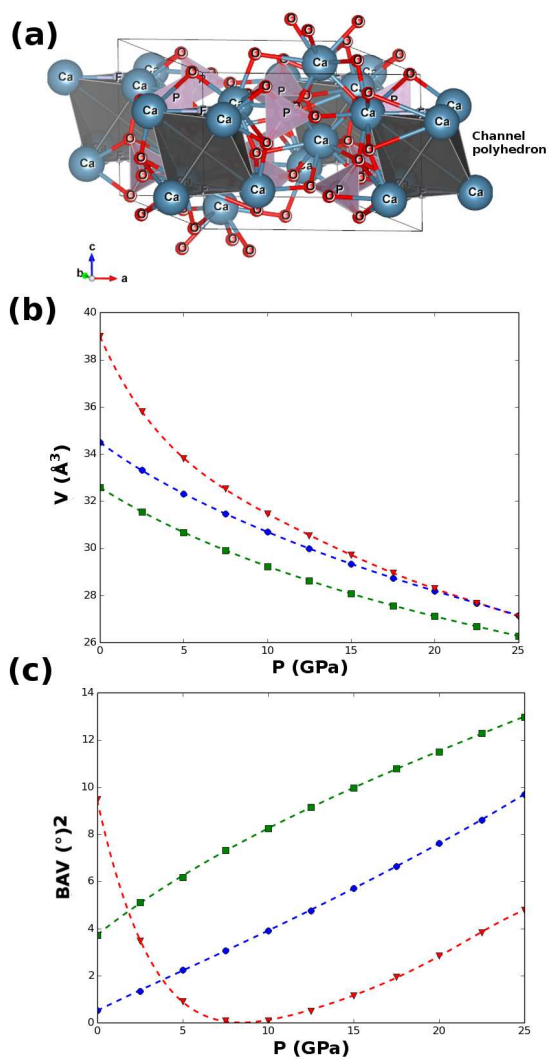
Fig. 4 (a) Unit cell of fluorapatite with the "channel polyhedron" (defined in the text) highlighted. The pressure dependence of the (b) volumes, and (c) bond angle variances (BAV) of the channel polyhedra in FAP (squares), HAP (circles), and CAP (inverted triangles) are also shown

639
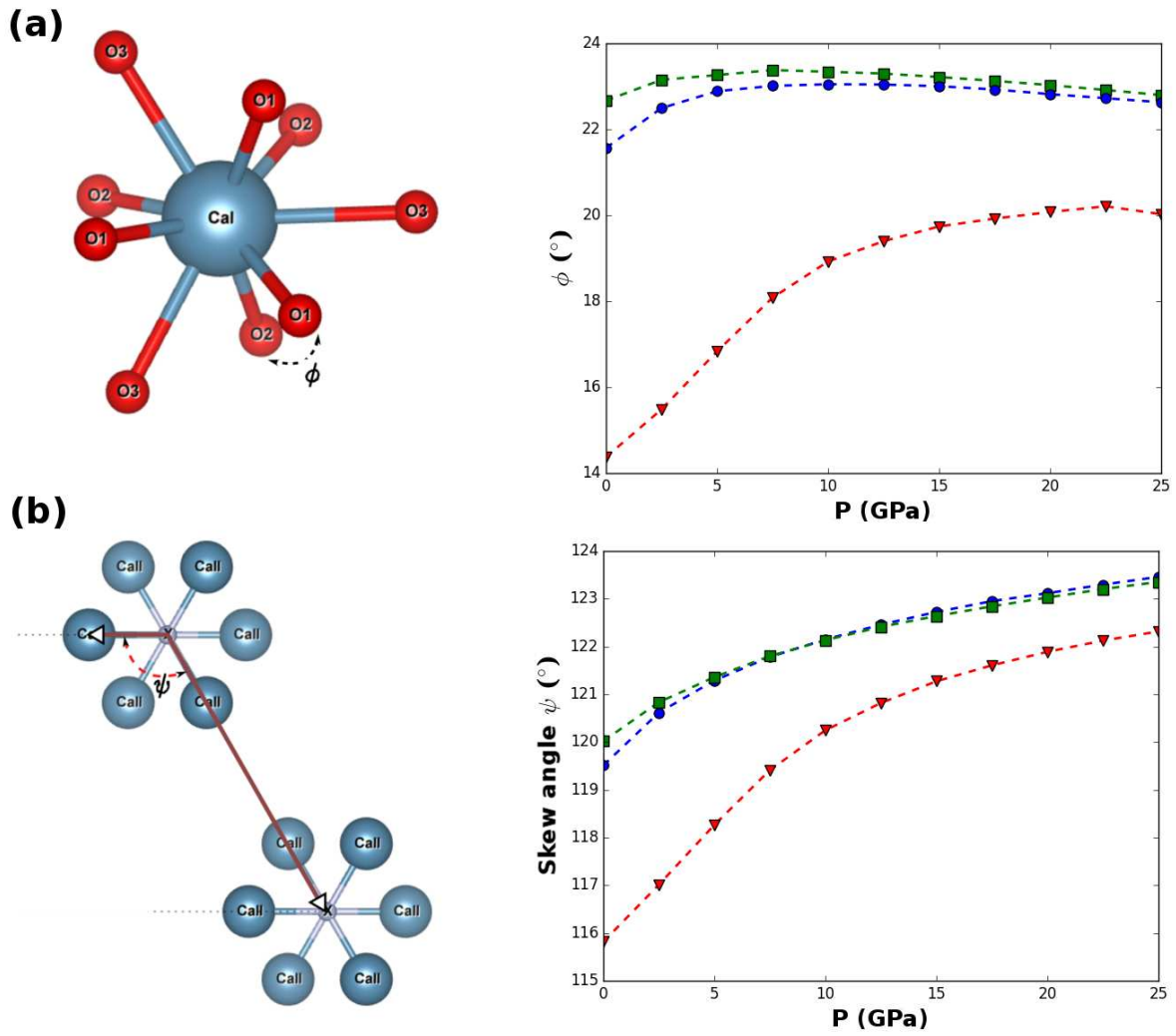
Fig. 5 Illustrations of (a) the metaprism twist ϕ and (b) the skew angle ψ, together with their

calculated pressure dependences, for FAP (squares), HAP (circles), and CAP (inverted triangles)

642
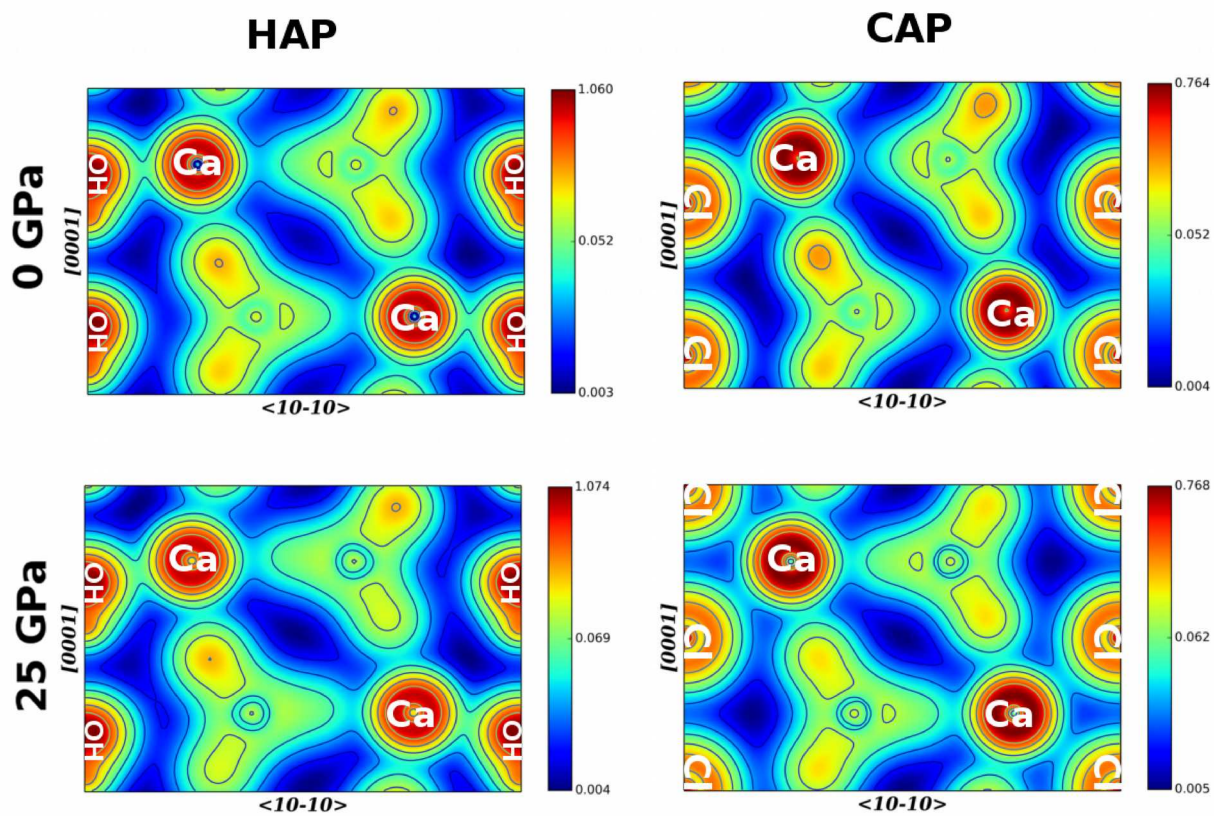
Fig. 6 Calculated valence electron densities at 0 GPa and 25 GPa for HAP and CAP
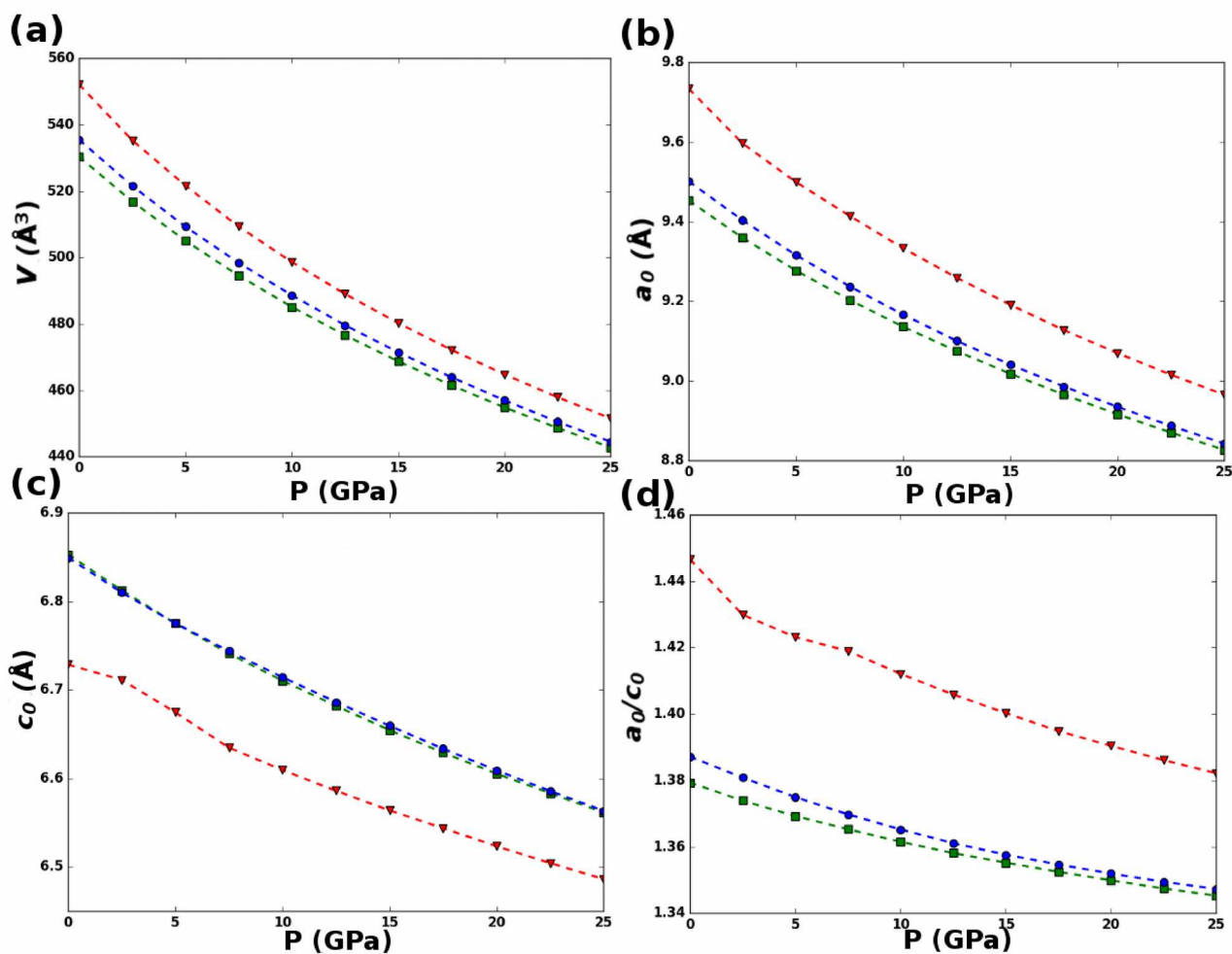
Fig. 7 Pressure dependence of the (a) cell volumes, (b) a_0 cell parameter, (c) c_0 cell parameter, and (d) a_0/c_0 ratio of FAP (squares), HAP (circles), and CAP (inverted triangles) calculated with dispersion forces treated using the DFT-D2 scheme
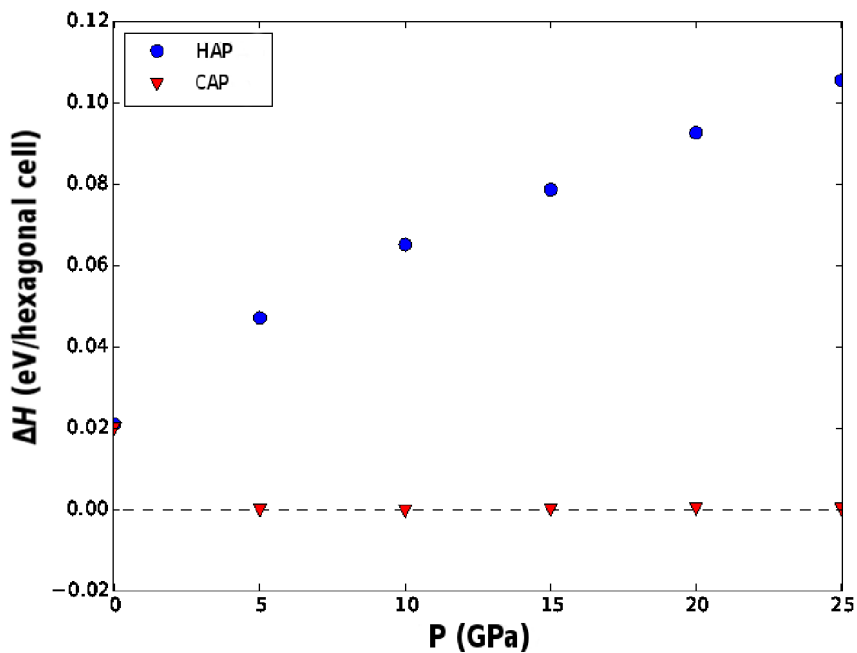
648

649 **Fig. 8** Plot of ΔH (per hexagonal cell) against pressure, for the phase transition from the monoclinic

650 to hexagonal forms of HAP (circles) and CAP (inverted triangles)
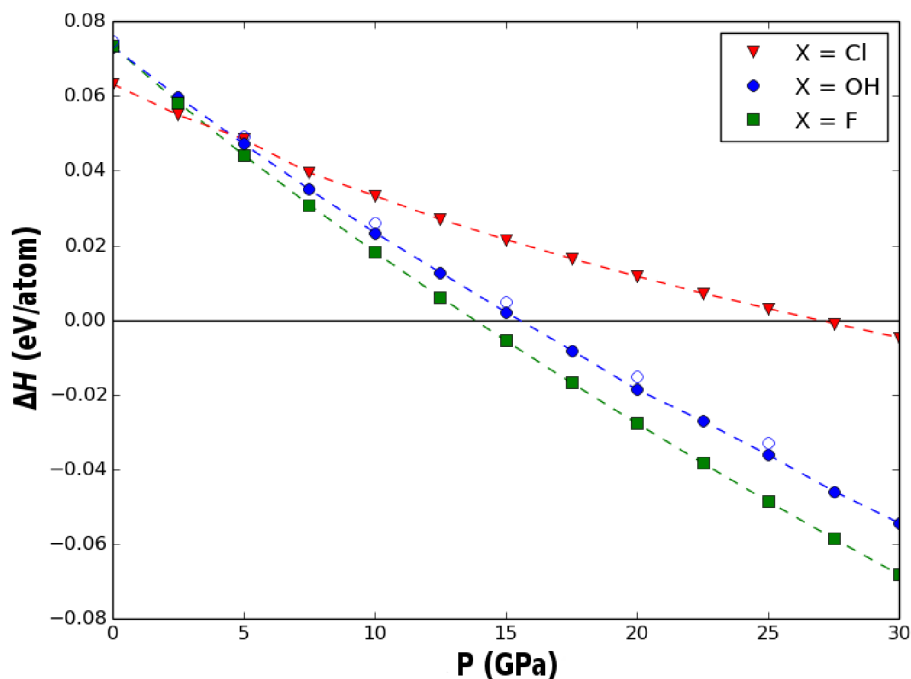
651

652 **Fig. 9** Calculated ΔH (per atom), obtained using DFT, for the decomposition of FAP (squares), HAP

653 (circles), and CAP (inverted triangles) to produce tuite and CaX_2 (X=F, OH, Cl). Hollow symbols

654 give the reaction enthalpy for monoclinic HAP

655   **Table 1** Calculated cell volumes and *a* and *c* cell parameters for FAP, HAP, and CAP as functions of

656   pressure

P (GPA)	FAP			HAP			CAP		
	V (Å³)	a_0 (Å)	c_0 (Å)	V (Å³)	a_0 (Å)	c_0 (Å)	V (Å³)	a_0 (Å)	c_0 (Å)
0.0	542.74	9.518	6.917	549.52	9.592	6.896	573.07	9.900	6.751
2.5	527.25	9.407	6.880	532.95	9.464	6.871	549.66	9.730	6.704
5.0	514.30	9.317	6.841	519.27	9.363	6.840	531.85	9.588	6.680
7.5	502.86	9.236	6.808	507.57	9.278	6.808	517.71	9.468	6.668
10.0	492.73	9.165	6.774	497.21	9.204	6.777	505.76	9.369	6.654
12.5	483.54	0.100	6.742	487.74	9.136	6.748	495.49	9.286	6.635
15.0	475.43	9.043	6.714	479.20	9.074	6.720	486.20	9.213	6.614
17.5	467.86	8.989	6.687	471.39	9.018	6.694	477.73	9.147	6.593
20.0	460.97	8.939	6.661	4.64.19	8.966	6.668	470.16	9.088	6.573
22.5	454.38	8.891	6.637	4.57.44	8.916	6.644	463.17	9.034	6.554
25.0	448.25	8.846	6.614	451.12	8.870	6.621	456.66	8.984	6.533

657

658 **Table 2** BM3 EOS parameters for hexagonal FAP, HAP, and CAP

	K_0 (GPa)	K_0'	V_0 (Å^3)	K_0	V_0 (Å^3)
FAP	82.1(11)	4.9(1)	542.6(3)	90.7(19) **(97.9)**	540.8(12) **(522.4)**
HAP	79.2(14)	4.8(2)	549.1(5)	87.1(17) **(97.5)**	547.4(12) **(526.9)**
CAP	55.0(20)	6.3(3)	572.3(10)	73.9(42)	566.2(39)

659 The last two columns are the 0 GPa bulk modulus and cell volume with K_0' set equal to 4.0.

660 Values in bold are fits to experimental data in Brunet et al. (1999). While Brunet et al. did not

661 compress a sample of ClAp, they did compress an apatite with composition $Ca_5(PO_4)_3Cl_{0.7}(OH)_{0.3}$,

662 which had K_0= 93.1 GPa and V_0 = 539.4 Å^3

663 **Table 3** Cell volumes and a_0 and c_0 cell parameters for FAP, HAP, and CAP calculated as functions

664 of pressure with the dispersion forces treated using the DFT-D2 scheme

P (GPA)	FAP			HAP			CAP		
	V (Å^3)	a_0 (Å)	c_0 (Å)	V (Å^3)	a_0 (Å)	c_0 (Å)	V (Å^3)	a_0 (Å)	c_0 (Å)
0.0	530.32	9.453	6.853	535.47	9.501	6.849	552.09	9.734	6.729
2.5	516.83	9.360	6.813	521.53	9.404	6.810	535.28	9.597	6.711
5.0	505.02	9.277	6.775	509.25	9.316	6.775	521.64	9.500	6.675
7.5	494.52	9.204	6.741	498.37	9.238	6.744	509.30	9.415	6.634
10.0	485.10	9.136	6.710	488.63	9.167	6.714	498.62	9.333	6.610
12.5	476.57	9.075	6.682	479.60	9.101	6.686	489.01	9.259	6.586
15.0	468.71	9.018	6.654	471.44	9.031	6.660	480.24	9.191	6.564
17.5	461.48	8.965	6.629	463.92	8.986	6.634	472.16	9.128	6.544
20.0	454.80	8.917	6.605	456.96	8.935	6.609	464.76	9.070	6.523
22.5	448.61	8.871	6.583	450.47	8.887	6.586	457.87	9.016	6.486
25.0	442.72	8.827	6.561	444.46	8.842	6.563	451.47	8.965	6.469

665

666   **Table 4** BM3 EOS parameters calculated for hexagonal FAP, HAP, and CAP using the cell volumes

667   calculated using the DFT-D2 scheme. The last two columns are the 0 GPa bulk modulus and cell

668   volume with $K_0^{'}$ set equal to 4.0

	K_0 (GPa)	$K_0^{'}$	V_0 (Å^3)	K_0	V_0 (Å^3)
FAP	91.7(2)	4.5(1)	530.3(1)	98.2(6)	529.0(4)
HAP	88.7(3)	4.4(1)	535.6(1)	93.6(5)	534.5(3)
CAP	78.4(4)	4.6(1)	551.7(1)	85.3(7)	549.9(5)

669